

QUARTERLY JOURNAL
OF THE
ROYAL METEOROLOGICAL SOCIETY

Vol. 127

JANUARY 2001 Part A

No. 571

Q. J. R. Meteorol. Soc. (2001), **127**, pp. 1–24

Exploring natural and anthropogenic variation of climate

By S. MANABE¹*, T. R. KNUTSON², R. J. STOUFFER² and T. L. DELWORTH²

¹*Frontier Research System for Global Change, Japan*

²*Geophysical Fluid Dynamics Laboratory/NOAA, USA*

(Received 7 July 2000; revised 15 August 2000)

(Symons Memorial Lecture: delivered by S. Manabe on 17 May 2000)

SUMMARY

This lecture discusses the low-frequency variability of surface temperature using a coupled ocean–atmosphere–land-surface model developed at the Geophysical Fluid Dynamics Laboratory/NOAA. Despite the highly idealized parametrization of various physical processes, the coupled model simulates reasonably well the variability of local and global mean surface temperature. The first half of the lecture explores the basic physical mechanisms responsible for the variability. The second half examines the trends of local surface temperature during the last half century in the context of decadal variability simulated by the coupled model.

KEYWORDS: Climate change Climate modelling Low-frequency variability

1. INTRODUCTION

Using a coupled ocean–atmosphere–land-surface model developed at the Geophysical Fluid Dynamics Laboratory/NOAA†, this lecture explores the physical mechanisms of climate variability based upon the comparative assessment of the observed and simulated variability of surface temperature.

Figure 1 illustrates the time series of globally averaged, annual mean surface air temperature (SAT) anomalies which was compiled at the University of East Anglia, UK (Jones and Wigley 1991). It exhibits temporal variation of global mean SAT with interannual, decadal, interdecadal and multidecadal time-scales. The figure also indicates a positive trend during the twentieth century. The first part of this paper explores the physical mechanisms responsible for local and global surface temperature variations, based mainly upon the study of Manabe and Stouffer (1996).

The second part of this paper assesses the observed trend of local surface temperature during the last half century. Figure 2 illustrates the local linear trend of annual mean surface temperature between 1950 and 1998 (Hansen *et al.* 1999). This figure indicates that, during the last half century, particularly large warming has occurred over Siberia and Alaska, and modest warming over the Indian and eastern tropical Pacific Oceans. Of particular interest is the cooling of significant magnitude which has occurred over the northern North Atlantic and North Pacific Oceans. Using diagnostic analyses of observed and simulated trends and variability of surface temperature (e.g. Knutson and Manabe 1998; Knutson *et al.* 1999), we explore and assess the physical mechanisms which may be responsible for these trends.

* Corresponding author: Frontier Research System for Global Change, 7F Seavans-North Bldg, 1-2-1 Shibaura, Minato-Ku, Tokyo 105-6791, Japan. e-mail: sm@frontier.esto.or.jp

† National Oceanic and Atmospheric Administration.

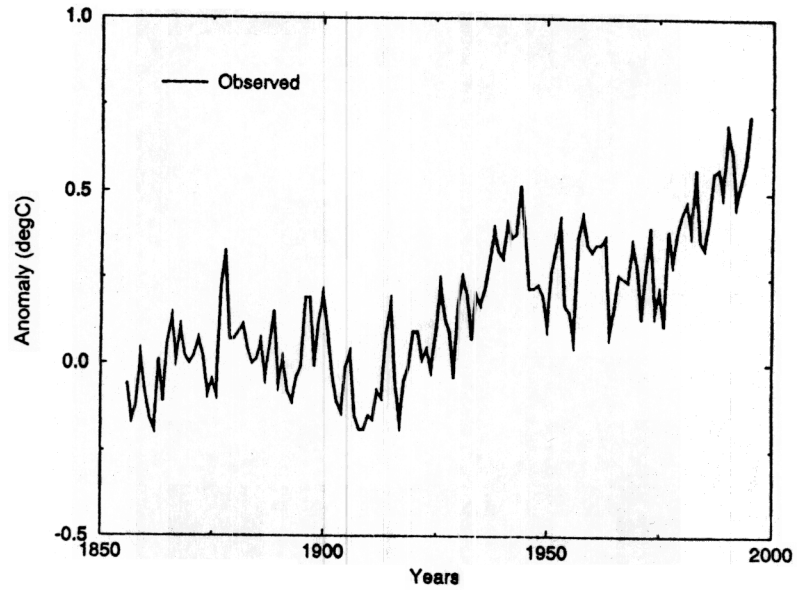


Figure 1 Time series of globally averaged, annual mean surface air temperature anomalies (i.e. the deviation from the 1880 to 1920 mean) (Jones and Wigley 1991).

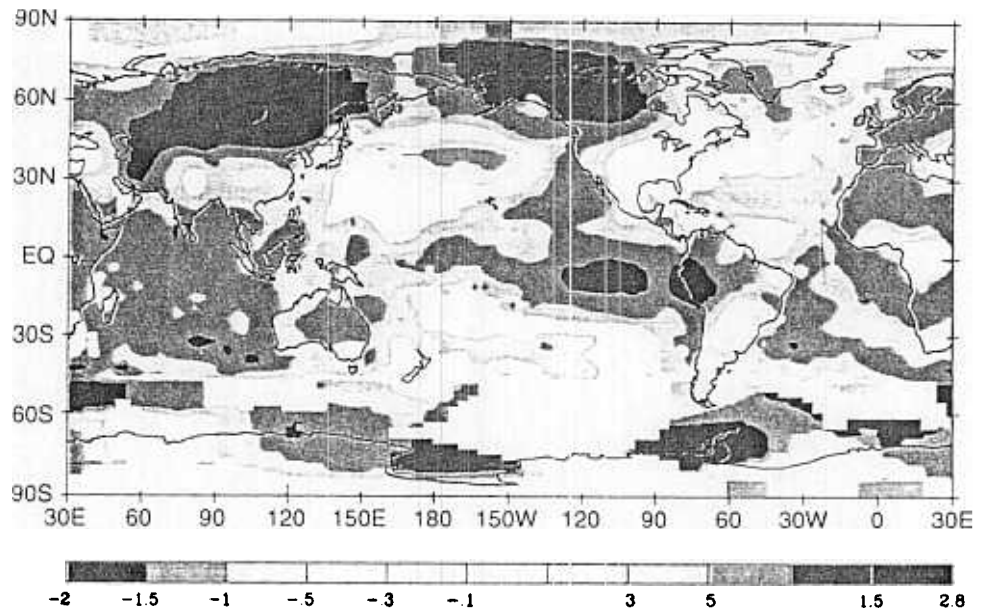


Figure 2. Change of annual mean surface temperature index (degC) for the period 1950–98 based on local linear trends which are computed from surface air temperature change over land and sea surface temperature (SST) change over the ocean (Reynolds and Smith 1994). The SST change is determined based upon ship measurements for the period 1982–98 and upon both ship measurements and an empirical orthogonal function analysis for the period 1950–81 (Smith *et al.* 1996). From Hansen *et al.* (1999).

2. COUPLED MODEL

(a) *Model structure*

The model used here is described in detail by Manabe *et al.* (1991). It consists of general-circulation models (GCMs) of the atmosphere and oceans, and a simple model of continental surfaces. It is a global model with realistic geography limited by its computational resolution. It has nine vertical finite-difference levels. The horizontal distributions of predicted variables are represented by spherical harmonics of 15 associated Legendre functions for each of 15 Fourier components (rhomboidal 15 truncation) and by grid-point values (Gordon and Stern 1982). The vertical transfer of sensible and latent heat through moist convection is represented by a simple scheme called 'moist convective adjustment' (Manabe *et al.* 1965). Insolation varies seasonally, but not diurnally. The model predicts cloud cover, which depends only on relative humidity. A simple bucket model of the continental surface is used to compute the budget of water and heat (Manabe 1969).

The oceanic GCM (Bryan and Lewis 1979) uses a finite-difference technique and has a regular grid system with approximately a 4° latitude \times 3.7° longitude spacing. There are 12 vertical finite-difference levels. The atmospheric and oceanic components of the model interact with each other once each day through the exchange of heat, water, and momentum fluxes. A simple sea-ice model is also incorporated into the coupled model. It predicts only sea-ice thickness computed from a thermodynamic heat balance and the advection of ice by surface ocean currents. For further details about the model, which is going to be called the 'coupled model' for simplicity, see Manabe *et al.* (1991).

The model just described incorporates some of the simplest parametrizations of various physical processes involved, facilitating the interpretation of model behaviour. Although the computational resolution of the model is low, it permits daily weather disturbances with realistic amplitude. Some of the results discussed in the latter part of this paper (Knutson and Manabe 1998; Knutson *et al.* 1999) are obtained from versions of the coupled model that have a resolution approximately twice as fine as the coupled model described above.

(b) *Numerical time integration*

The initial condition for the time integration of the coupled model was obtained from separate time integrations of the atmospheric and oceanic components of the model. For the integration of the atmospheric component of the model, the observed distribution of sea surface temperature (SST) with seasonal variation was used as a lower boundary condition. For the integration of the oceanic component, the observed distributions of SST and surface salinity, together with the distribution of wind stress, which is obtained from the integration of the atmospheric component of the model mentioned earlier, are used as upper-boundary conditions. Both integrations were performed long enough to reach a state of quasi-equilibrium. Starting from the initial condition obtained by combining the quasi-equilibrium states of the atmospheric and oceanic components, the coupled model was integrated for more than 1000 model years and was extended later up to 14 000 years.

When the time integration of a coupled model starts from the initial conditions identified earlier, the model climate often drifts toward its own less realistic equilibrium state. To reduce such drift, the fluxes of heat and water at the ocean-atmosphere interface are adjusted by given amounts before they are imposed upon the oceanic surface (see Manabe *et al.* (1991) for details). These adjustments do not change from one year to the next and are independent of the anomalies of temperature and salinity at the oceanic

surface, which fluctuate during the time integration of the coupled model. Thus, they neither systematically damp nor amplify surface anomalies. Although the adjustments do not eliminate the shortcomings of model dynamics or thermodynamics (Marotzke and Stone 1995), they do help prevent the drift of the model from the realistic initial state. Such drift can seriously distort the sensitivity and variability of model climate.

Obviously, it is highly desirable to develop a coupled model that can maintain a realistic control climate in the absence of flux adjustments (Gregory and Mitchell 1997; Gordon *et al.* 2000). However, in trying to obtain a realistic climate without flux adjustment, one has to guard against the possibility of overtuning one component of the model to make up for shortcomings in other components.

(c) *The mixed-layer model*

In order to elucidate the effect of ocean currents upon the variability of climate, we constructed another model in which the atmospheric GCM is combined with a simple mixed-layer ocean model consisting of a vertically well-mixed slab layer of ocean with uniform thickness of 50 m. This model, which is called the 'mixed-layer model' for the sake of simplicity, does not have the effects of oceanic thermal advection and diffusion, which are included in the coupled model described earlier. Comparing variability of the coupled and mixed-layer models, it is possible to identify the effect of changes in the oceanic heat transport upon SST variability.

The model contains an idealized scheme for sea-ice prediction, which is identical to the scheme in the coupled model described earlier except that it does not include horizontal advection of sea ice by ocean currents. As proposed by Hansen *et al.* (1984), the rate of heat exchange between the mixed layer and deeper layers of the ocean is prescribed such that the seasonal and geographical distribution of SST and sea-ice thickness are as realistic as possible. Again, one should note here that this prescribed heat flux is determined before the integration of the mixed-layer model, and is not correlated systematically with the SST anomalies which fluctuate during the course of the time integration of the mixed-layer model. Therefore, it is not likely that the prescribed heat fluxes systematically damp or amplify the SST anomalies. Owing to the prescribed heat flux described here, the climatological distribution of SST remained realistic throughout the course of the 1000-year integration conducted.

3. SURFACE TEMPERATURE VARIABILITY

(a) *Local variability*

Before discussing the temporal variability of global mean SAT shown in Fig. 1, we begin with a description of the low-frequency variability of local SAT in the 1000-year integrations of the coupled model obtained by Manabe and Stouffer (1996). Figure 3 compares the simulated and observed distribution of the standard deviation of local, annual mean SAT. The figure indicates that the simulated SAT variability is substantially larger over the continents than oceans, in agreement with the observations. Because the simulated amplitude of El Niño/Southern Oscillation (or ENSO) is less than half of that observed (Knutson *et al.* 1997), the model underestimates the SAT variability in the eastern tropical Pacific. Nevertheless, this figure clearly demonstrates that the model reproduces approximately the interannual variability of local SAT.

A similar comparison is also made for local, 5-year mean SAT (Fig. 4). Again, the agreement between the simulated and observed distributions is good, indicating that the coupled model reproduces approximately observed decadal SAT variability.

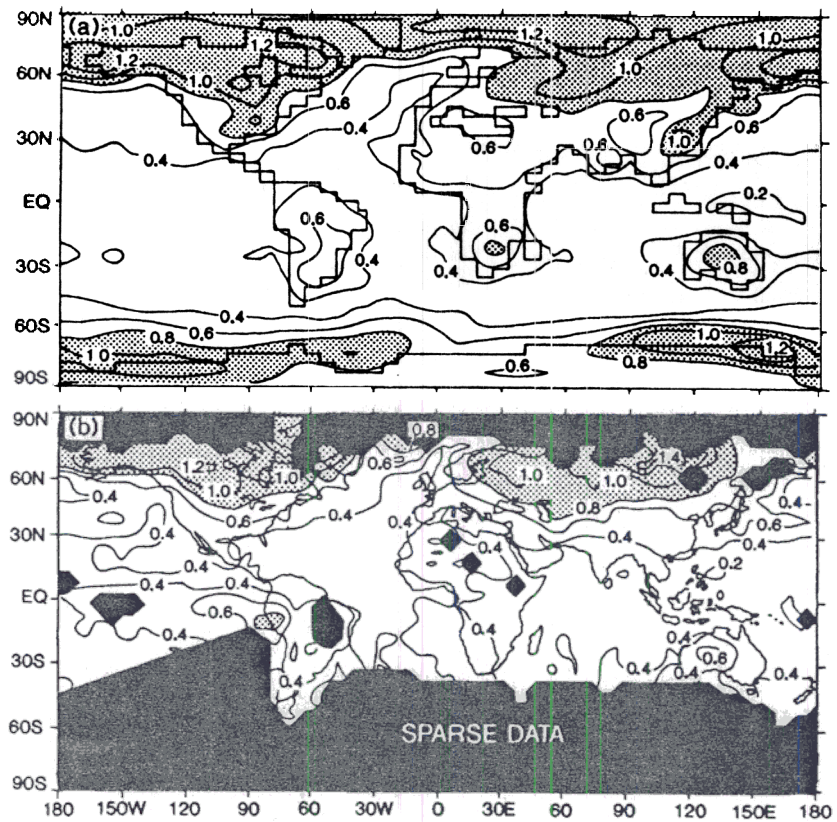


Figure 3. Geographical distribution of the standard deviation of annual mean surface air temperature (SAT) anomaly (degC): (a) simulated by the coupled model, and (b) observed (computed using the data compiled by Jones and Wigley (1991)). From Manabe and Stouffer (1996).

In order to explore the role of oceanic heat transport in generating the local SAT variability described above, we conducted a 1000-year integration of the mixed-layer model described in the preceding section. Figure 5 illustrates the geographical distribution of SAT obtained from this integration. Comparing the standard deviation of SAT from the mixed-layer model (Fig. 5) with that from the coupled model (Fig. 3(a)), we hoped to determine the influence of changes in oceanic heat transport upon SAT variability. Despite the fact that the amplitude of simulated ENSO has about 45% of the observed amplitude, the standard deviation of SAT variability in the equatorial region of the eastern tropical Pacific in the coupled model is larger than that of the mixed-layer model. Otherwise, the geographical distribution of annual mean SAT variability is similar between the two models. It appears that, with the exception of the eastern tropical Pacific, where SST fluctuates significantly due to the Southern Oscillation, oceanic heat transport has relatively little effect upon the simulated, interannual variability of local SAT.

A similar comparison was made for the variability of 5-year mean SAT (see Fig. 2 of Manabe and Stouffer (1996)). Again, the geographical distribution of variability is similar between the coupled and mixed-layer models. This indicates that, in general, oceanic heat transport has a relatively small effect upon the decadal variability of local SAT. (See Stouffer *et al.* (2000) for a description of SAT variability in the time

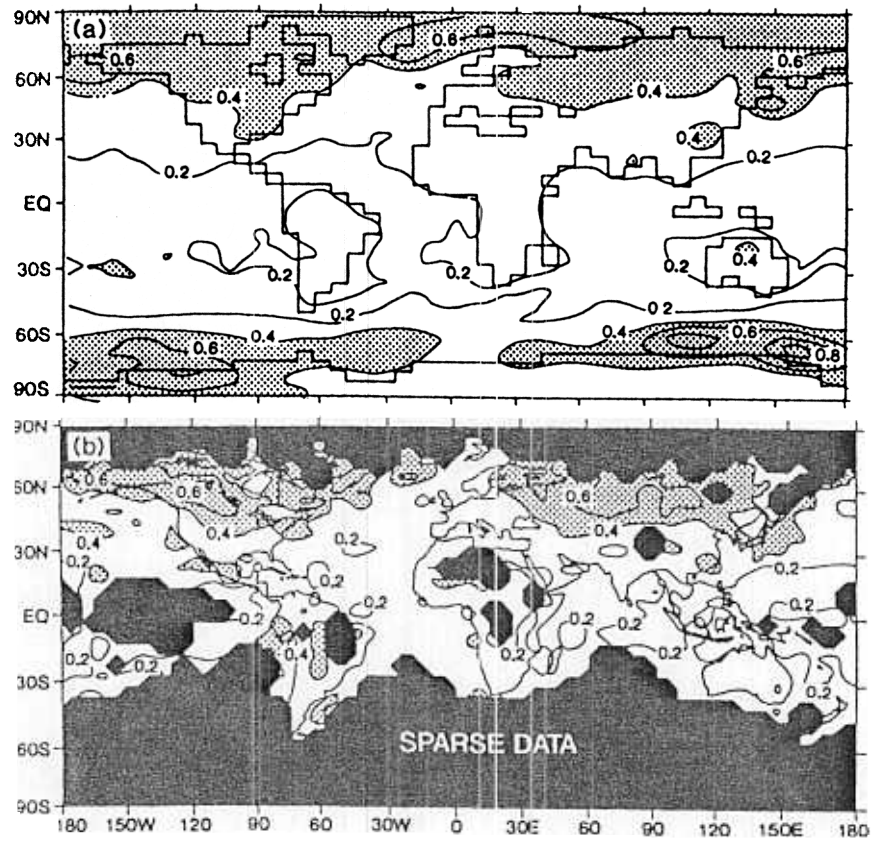


Figure 4. Same as Fig. 3 but for 5-year mean SAT anomalies. From Manabe and Stouffer (1996).

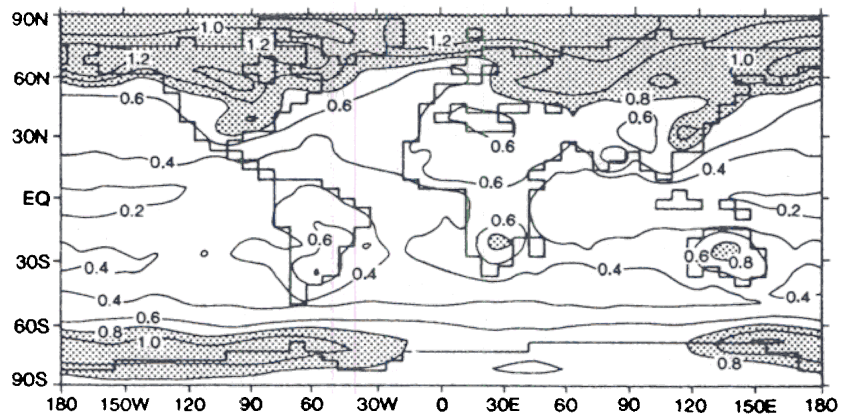


Figure 5. Geographical distribution of the standard deviation of annual mean surface air temperature anomaly (degC) simulated by a 1000-year integration of the mixed-layer model. From Manabe and Stouffer (1996).

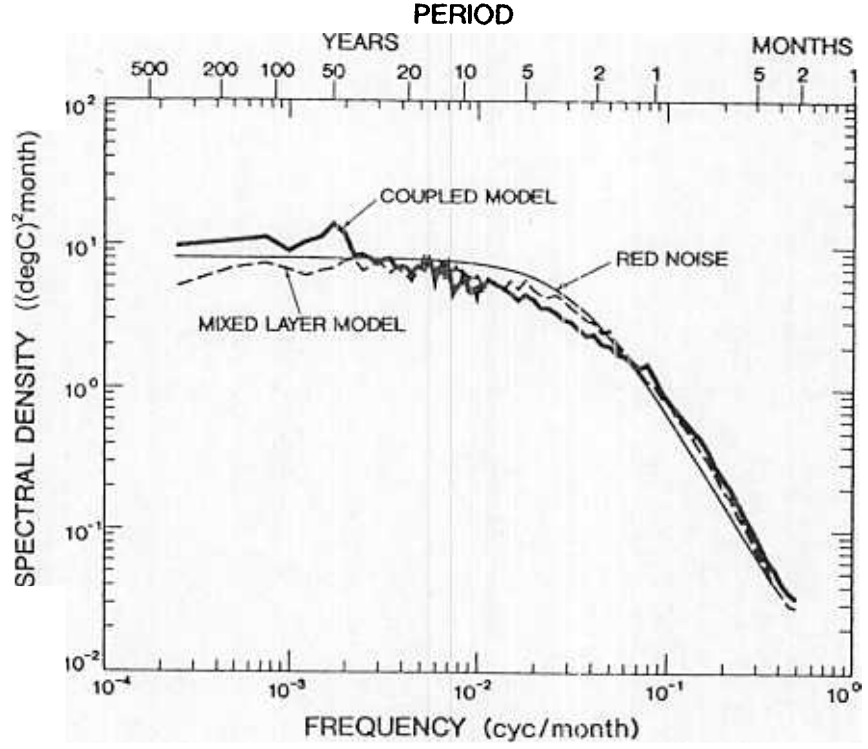


Figure 6. Power spectrum of monthly mean sea surface temperature anomaly obtained from the coupled model (thick dashed line), and mixed-layer model (thin dashed line). Both spectra are obtained by averaging the spectra at all grid points, which are located in the mid oceanic boxes of the North Pacific (28.9°N–42.2°N, 155.6°E–140.1°W) and North Atlantic (28.9°N–42.2°N, 61.9°E–28.1°W). The thin solid line is the red-noise spectrum: the least-square fit to the coupled model spectrum, obtained from Manabe and Stouffer (1996). Note, however, that the unit of the ordinate is corrected to be (degC)² month here rather than (degC)² year which was incorrectly used in all illustrations of spectra in the paper of Manabe and Stouffer (1996).

integrations of other coupled models which were developed at the Hadley Centre (United Kingdom), and Max Planck Institute for Meteorology (Germany).)

(b) *Linear stochastic model*

Hasselmann (1976) proposed a 'linear stochastic model' of SST variability, providing an excellent foundation for the development of the theory of climate variability. He noted that, in the mid-oceanic regions away from the coastal boundaries, the temporal variation of surface temperature of the mixed-layer ocean may be regarded as the red-noise response to random, white-noise forcing by synoptic scale, weather disturbances.

The governing equation of the linear stochastic model may be written as:

$$C \frac{dT'}{dt} = f_w - \gamma T' \quad (1)$$

where T' is the SST anomaly, t is time, C is the heat capacity of the mixed-layer ocean, f_w is white-noise thermal forcing from the atmosphere, and γ is the rate of thermal damping due to radiative transfer, and sensible- and latent-heat fluxes. The power spectrum of SST response over the entire spectral range may be given by

$$G(\omega) = (F_0/C)^2 / \{(\gamma/C)^2 + \omega^2\} \quad (2)$$

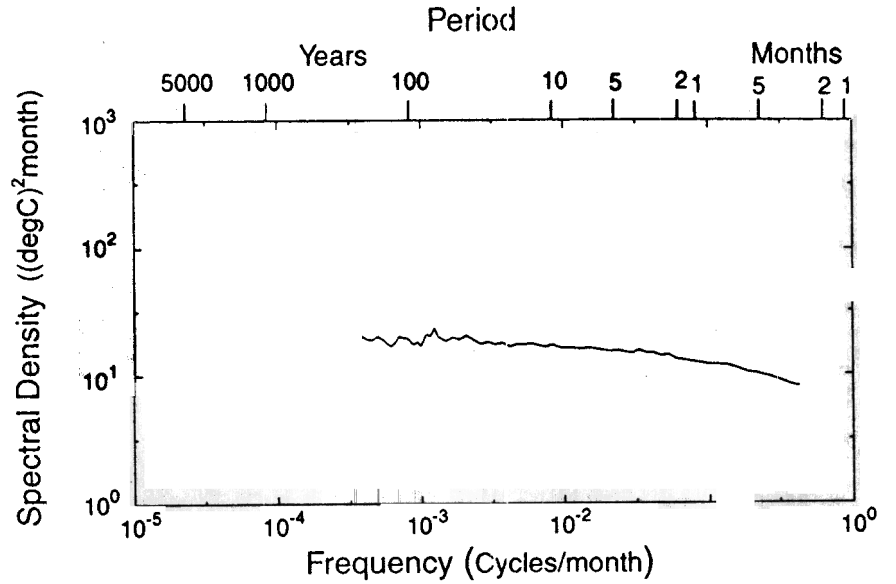


Figure 7. Power spectrum of land surface temperature anomalies obtained from the coupled model. The spectrum is obtained by averaging the spectra over all continental grid points which are located between 30°N and 60°N.

where F_0 is the amplitude of the white-noise forcing, and ω is angular velocity, which is equal to $2\pi \times$ frequency.

An example of this red-noise spectrum is shown in Fig. 6. At high frequencies, the contribution from $\gamma T'$ is relatively small in Eq. (1). Thus, $C dT'/dt$ balances f_w , yielding the (-2) slope. At low frequencies, the contribution of $C dT'/dt$ becomes relatively small. Thus, f_w balances $\gamma T'$, yielding a white-noise response which is constant with respect to frequency. The time-scale of the transition from the (-2) slope to the constant spectral density of white noise is given by C/γ . The period of separation between the two regimes is around three years for the mixed-layer ocean.

Figure 6 also contains the SST spectra of both the coupled and mixed-layer models. These are obtained by averaging the spectra of all grid points in the mid-oceanic boxes in the North Pacific and North Atlantic Oceans. The spectra of both models, which are similar to each other, fit well to the red-noise spectrum shown in the same figure. This implies that the theory of the linear stochastic model is valid in the extratropical, mid-oceanic regions of both coupled and mixed-layer models. The similarity between the two spectra also implies that the contribution of oceanic heat transport to the SST variability appears to be small in these regions.

Hall and Manabe (1997) analysed the observed time series of SST and sea surface salinity (SSS) at weather station Papa located in the north-western North Pacific (51.8°N, 148.1°W). The spectra of both SST and SSS time series fit reasonably well to a red-noise spectrum in conformity with the linear stochastic model. However, the SSS spectrum is significantly redder than the SST spectrum, underscoring the weaker damping of SSS as compared with SST anomalies. As one may expect, an SST anomaly is damped much faster than an SSS anomaly.

Over the continental surface where the effective heat capacity C is small, the separation time-scale C/γ is also small, yielding essentially a white-noise response to the white-noise forcing from the atmosphere. Figure 7 illustrates a spectrum of land

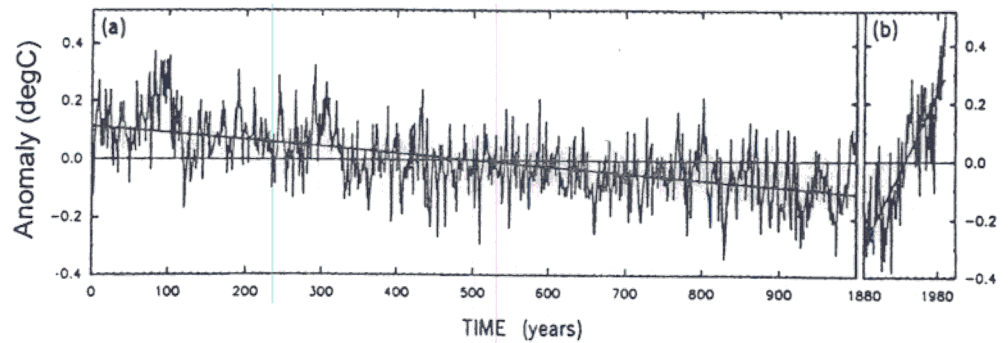


Figure 8. Time series of globally averaged, annual mean surface air temperature anomalies from a long-term mean: (a) 1000-year time series from the coupled ocean–atmosphere model and (b) 110-year (AD 1881–1990) time series of observed anomaly. The straight lines through both time series represent least-square fits.

surface temperature obtained by averaging the spectra of all continental grid points between 30°N and 60°N of the coupled model. It shows that the mean spectrum is white down to the time-scale of several months, conforming to the theory of the linear stochastic model.

The results presented in this and the previous section indicate that, with the exception of the tropical Pacific Ocean, the linear stochastic model can account for a major fraction of surface temperature variability over both continent and ocean. However, the SST spectrum deviates significantly from red noise at multidecadal time-scales in high latitude oceanic regions as discussed later.

(c) Global variability

The local SST variability discussed in the preceding subsection contributes to the variability of global mean SAT. Figure 8 illustrates the time series of globally averaged, annual mean SAT obtained from the 1000-year integration of the coupled model. It also shows the time series of observed, global mean SAT, indicating the average warming trend of about 0.5 degC per 100 years sustained during the twentieth century. The 1000-year time series of the coupled model exhibits temporal variation with interannual, decadal, interdecadal, and multidecadal time-scales. It contains sustained, positive or negative, trends that are as large as the observed trend of 0.5 degC per 100 years. However, as noted by Stouffer *et al.* (1994), such a trend is never sustained for longer than 60 years. (A similar statement holds when the time integration of the coupled model is extended to 14 000 years.) Provided that simulated variability is realistic, it is therefore not likely that the observed trend of 0.5 degC per 100 years sustained during the twentieth century is generated through internal mechanisms alone. Instead, it may have been induced at least partly by thermal forcing such as the increase of greenhouse gases in the atmosphere.

In order to evaluate how realistic the variability of the time series of the coupled model is, Fig. 9 is constructed. This figure contains the power spectrum of recently simulated 14 000-year time series of global mean SAT and that of the observed time series. (Both time series were detrended before the spectral analysis.) Over the periods which range from 30 years to a few thousand years, the simulated spectrum is essentially white, indicating that surface temperature anomalies have enough time to equilibrate with white-noise forcing from the atmosphere. However, at periods shorter than 30 years, the spectral density of global mean surface temperature decreases gradually

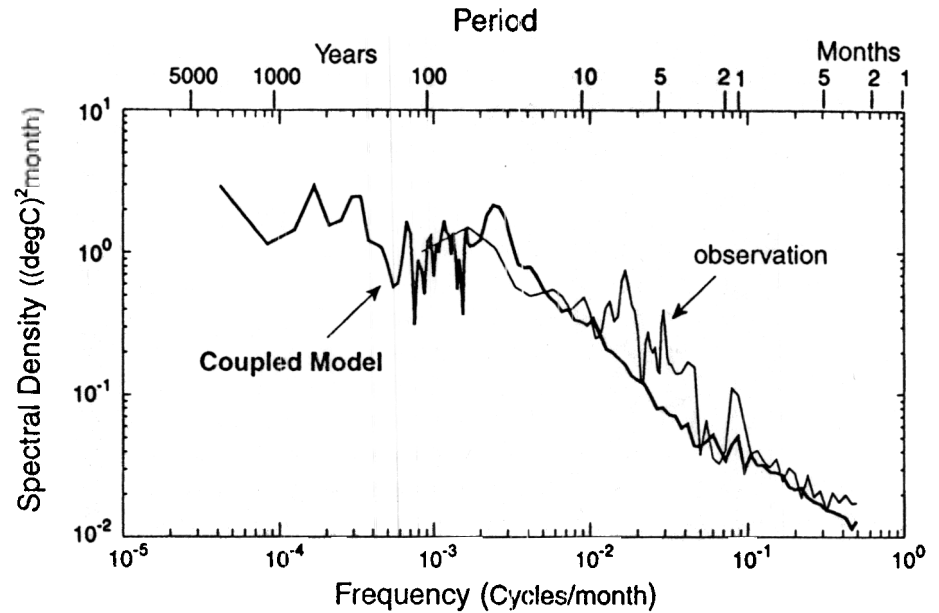


Figure 9. Power spectra of detrended globally averaged, monthly mean surface temperature anomalies. Thick solid line: the 14 000-year integration of the coupled model recently completed by Stouffer. Thin solid line: the observed 110-year (AD 1881–1990) time series compiled by Jones and Wigley (1991). This figure is similar to Fig. 17 of Manabe and Stouffer (1996) except that the length of the time integration of the coupled model is 14 000 rather than 1000 years. Note also that the unit of the ordinate is corrected to be $(\text{degC})^2 \text{ month}$ here rather than $(\text{degC})^2 \text{ year}$ which was incorrectly used in their study.

with increasing frequency, because the spatial scale of surface temperature anomalies decreases with increasing frequency. This differs substantially from the spectra of local surface temperature, which are white down to shorter periods as shown in Figs. 6 and 7. It is very encouraging that, with the exception of interannual time-scales, where the coupled model underestimates the amplitude of ENSO by a factor of more than two, the simulated spectrum agrees reasonably well with the observed.

4. COOLING TRENDS

In the introduction, we showed Fig. 2 illustrating the global distribution of local trends of surface temperature during the latter half of this century. One of the most notable features of the figure was the existence of cooling trends of substantial magnitude in the northern North Atlantic and North Pacific Oceans. In this section, we shall evaluate the recent trends of surface temperature based upon the studies of decadal variation of surface temperature that appeared in the long-term coupled model integrations.

(a) North Atlantic Ocean

Delworth *et al.* (1997) found large multidecadal variation of SST in the Denmark Strait when they analysed the results from a time integration of the coupled model. Figure 10 illustrates the 2000-year time series of low-pass filtered SST anomaly in the Denmark Strait, where the multidecadal SST variation is particularly pronounced. It indicates that the SST anomalies have a maximum/minimum range of about 4 degC. A spectral analysis of the SST time series illustrated in Fig. 11 indicates enhanced spectral

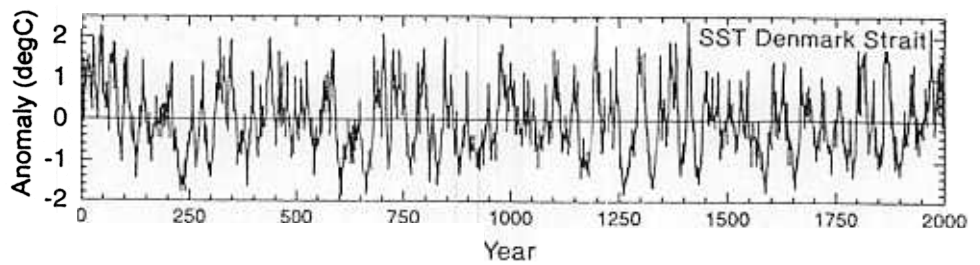


Figure 10. Time series of annual mean sea surface temperature (SST) in the Denmark Strait (15°W to 26°W at 70°N). Before plotting, the time series is filtered such that time-scales shorter than 10 years are effectively removed. The values are anomalies from the long-term mean of 0.62°C . From Delworth *et al.* (1997).

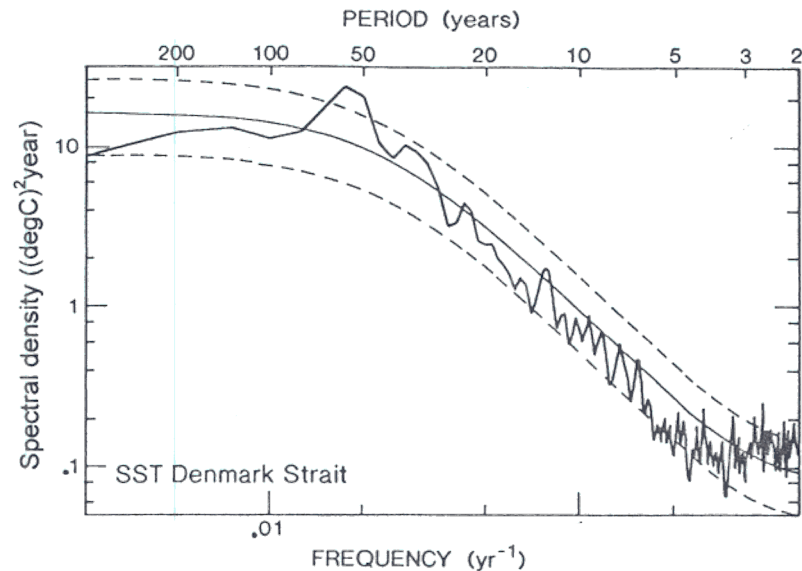


Figure 11. Spectrum of the time series of annual mean sea surface temperature (SST) of the coupled model in the Denmark Strait (15°W to 26°W at 70°N ; this is the time series shown in Fig. 10 before the filtering). The thin solid line denotes the spectrum of a background first-order Markov process, and the dashed line denotes the 95% confidence interval about that background spectrum. From Delworth *et al.* (1997).

density around 40–80 years. It has a statistically significant ($<5\%$) peak above a red-noise spectrum at about a 60-year period, thus deviating significantly from the linear stochastic model of Hasselmann.

The spatial pattern of SST anomaly, when SST is coldest at the Denmark Strait, is shown in Fig. 12, which illustrates the regression between SST at each grid point with the SST time series at the Denmark Strait. The region of cold anomalies shown here broadly corresponds to the region of observed cooling trends around the southern half of Greenland during the last 50 years. (For observed trend, refer not only to Fig. 2 but also to Fig. 18(a) (to be discussed later) in view of the very poor coverage of SST data around Greenland. These two maps are obtained using somewhat different methods.)

The multidecadal fluctuation of SST described above is accompanied by a so-called Great Salinity Anomaly event such as that discovered by Dickson *et al.* (1988). To describe the space–time structure of this simulated event, Delworth *et al.* computed at various time lags the linear regression between SSS at each grid point versus the time

series of SST shown in Fig. 10. Figure 13 illustrates the distributions of the surface salinity anomaly when the SST is coldest. It shows the extension of the low-salinity pattern extending all the way to the northern North Atlantic with a maximum anomaly around the Denmark Strait. The vectors of surface current anomalies, shown in the same figure, indicate the marked intensification of the East Greenland Current around the Denmark Strait, which accompanies large negative SSS anomalies.

As illustrated in Fig. 4 of Delworth *et al.* (1997), negative SSS anomalies develop in the Arctic, subsequently propagating out of the Arctic, through the Greenland Sea and Denmark Strait, and into the Labrador Sea. The anomalies follow the subpolar gyre as they propagate back to the Norwegian Sea in a manner similar to the Great Salinity Event described by Dickson *et al.* (1988). Inspecting the time series of surface and subsurface salinity at the Faroe–Shetland Channel (Dooley *et al.* 1984), Dickson *et al.* noted that the Great Salinity Anomalies of 1968–82 were preceded by a similar event in the early years of this century around 1910.

Dansgaard *et al.* (1971) conducted power spectrum analysis of $\delta^{18}\text{O}$ time series of an ice core from Camp Century, Greenland. They noted spectral peaks at the time-scales of 80 and 180 years, underscoring the existence of multidecadal oscillations of SST and other related variables in the regions near the northern North Atlantic. Such 60–80 year variability is also seen in the analysis of a variety of proxy indicators of climate (Delworth and Mann 2000).

The simulated multidecadal oscillation of the coupled model described earlier is coherent with the temporal variation of the intensity of the thermohaline circulation (THC) of the Atlantic Ocean (Delworth *et al.* 1993). This is because the THC and the subarctic gyre see-saw with each other at multidecadal time-scales (e.g. Manabe and Stouffer 1999). When the North Atlantic Current retreats, associated with the weakening of the THC, the East Greenland Current intensifies, generating cold SST and associated Great Salinity Anomaly. On the other hand, when the North Atlantic Current intensifies and extends northwards, the East Greenland Current weakens and retreats, generating warm and saline surface anomalies around the Denmark Strait. The distribution of SST anomalies associated with the intensified THC resembles the pattern of SST difference between the warm period (1950–64) and cold period (1970–82) in the North Atlantic Ocean, which was obtained by Kushnir (1994). The cold period identified by Kushnir approximately corresponds to the periods of weak THC and Great Salinity Anomalies in the Atlantic Ocean.

The irregular oscillation of the THC with a time-scale of 40–80 years was noted by Delworth *et al.* (1993) in a long-term integration of the coupled model. The oscillation appears to be driven by the near-surface density anomalies in the sinking region of the North Atlantic Ocean. The density anomalies are, in turn, induced by fluctuations of the THC itself, as well as by transport of heat and salt associated with a horizontal gyre circulation (i.e. the recirculation from the North Atlantic Current towards the coast of Labrador). The transports accomplished by this gyre circulation appear to play a prominent role in salinity and temperature anomalies associated with the fluctuation in the THC. Their analysis suggested that the irregular oscillations in the THC intensity are primarily a result of oceanic processes, although the role of the atmosphere should be explored further. Based upon the analysis of a well-designed set of numerical experiments, Delworth and Greatbatch (2000) concluded that the multidecadal fluctuation of the THC may be regarded as an oceanic response to atmospheric white-noise forcing, although the air–sea interaction appears to enhance the variability. With the natural frequency of a multidecadal time-scale, the Atlantic THC is particularly sensitive to atmospheric forcing at that time-scale, yielding a peak around 60 years. For more thorough discussion,

which is based upon the detailed analysis of the mechanism involved in the oscillation of the THC of the coupled model, refer to the study of Delworth *et al.* (1993).

Deser and Blackmon (1993) conducted the analysis of SST and SAT over the North Atlantic Ocean. In addition to what they call 'Dipole mode of SST variability' associated with the 'North Atlantic Oscillation', they identified the 'Gulf Stream Mode', which may be associated with the multidecadal variability of the THC. For example, their analysis of surface temperature indicates that, during the period between 1950 and 1989, the Gulf Stream Mode weakens, suggesting the possible weakening of the North Atlantic Current and the possible intensification of the East Greenland Current.

The results presented here suggest that the average cooling trend over the northern North Atlantic during the last half century is attributable partly to the multidecadal seesaw between the Atlantic THC and the subarctic gyre. In addition, one has to recognize that the so-called North Atlantic Oscillation index has increased markedly during the last 30 years, indicating the intensification of surface westerly winds over the North Atlantic. The stronger winds extract additional heat from the upper layer of the ocean, thereby contributing to the reduction of SST in the region.

(b) *North Pacific Ocean*

In Fig. 2, one notes a triangular-shaped region of SST warming trends in the eastern tropical Pacific Ocean, which is straddled by the regions of cooling trend in the mid-latitude region of the North Pacific and the subtropical region of the South Pacific Ocean. This pattern resembles the pattern of decadal variability found by Zhang *et al.* (1997). On the other hand, Knutson and Manabe (1998) obtained a similar pattern of decadal variability from a 120-year integration of a coupled model that has twice as high resolution as the model described earlier. Here, we shall explore how the pattern is generated based upon the results of Knutson and Manabe (1998).

The patterns of observed and simulated decadal variability are compared with each other in Fig. 14. These are obtained by low-pass filtering the variations with time-scales shorter than 7.5 years (e.g. the interannual time-scale of ENSO) from the detrended time series of SST, conducting the empirical orthogonal function (EOF) analysis of the filtered SST, and subtracting the patterns of cold from warm years. Both patterns resemble the pattern of observed trend described in the preceding paragraph (Fig. 2). They show a triangular-shaped warm anomaly region extending from the west coasts of North and South America in the subtropics westwards to the date-line along the equator. In the northern hemisphere, the warm anomalies extend northwards along the west coast of North America, reaching the Gulf of Alaska. The warm anomalies are flanked, in the central and western part of the Pacific basin, by negative anomalies in the subtropics to middle latitude of both hemispheres. Although the model has unrealistically large positive anomalies at the equator near the date-line, the patterns of simulated and observed interdecadal variation resemble each other.

To explore the decadal variation of the SST anomalies described earlier, Knutson and Manabe (1998) analysed the decadal variation of heat content anomalies (Fig. 15). In a manner similar to ENSO on the interannual time-scale, warm SST anomalies in the central and eastern Pacific induce surface wind anomalies that gradually raise the thermocline and reduce the heat content anomaly in the west. These induced heat content anomalies, associated with the thermocline perturbation in the west, eventually progress eastward along the equator (Fig. 15), elevating the thermocline in the eastern Pacific, initiating the cold phase of ENSO. The meridional span of heat content anomalies is slightly wider and their propagation is three to four times slower than for ENSO. However, the decadal variability of these heat content anomalies is qualitatively similar

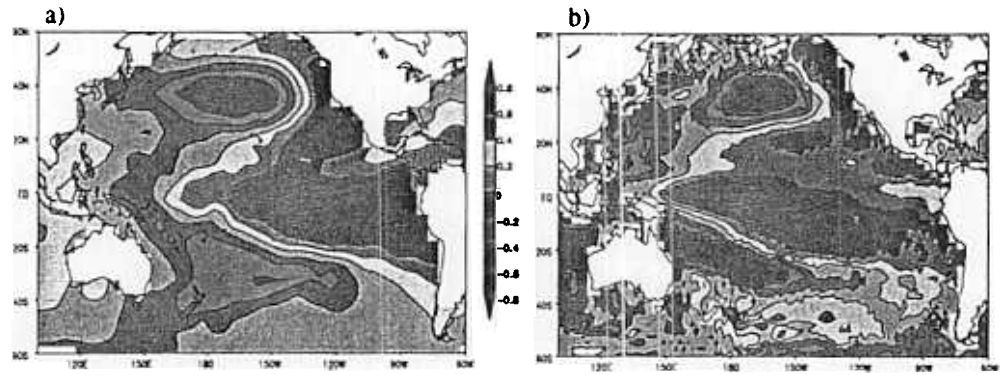


Figure 14. Decadal time-scale (>7 year, detrended) sea surface temperature composite (warm minus cold): (a) observed composite constructed using the GISST2.3 data set developed at the Hadley Centre (Rayner *et al.* 1996), and (b) as in (a) but based upon years 21–120 of a medium resolution coupled-model experiment. Contour interval is 0.2 degC. From Knutson and Manabe (1998).

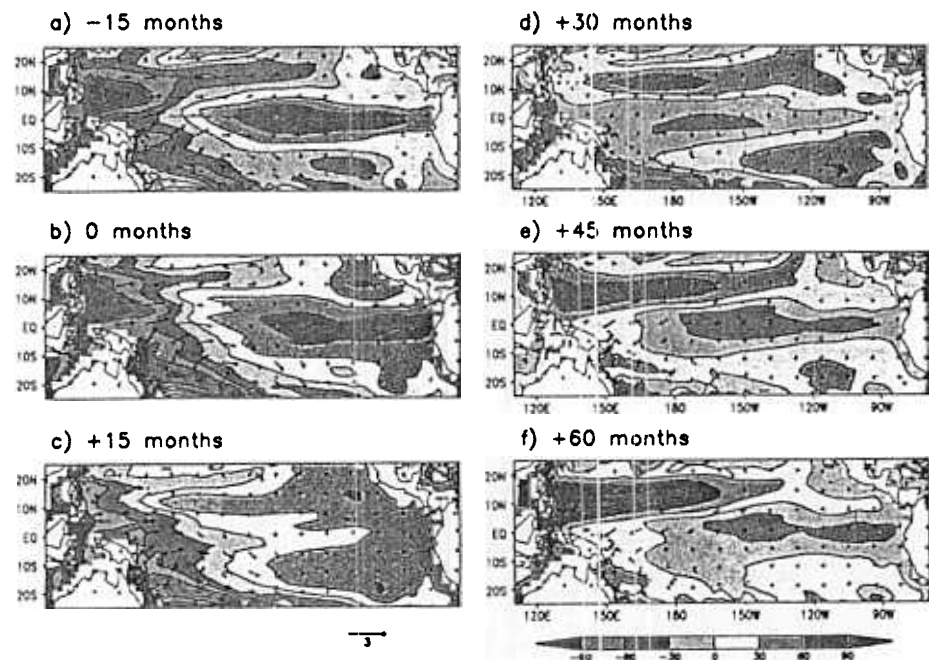


Figure 15. Time-lagged composite ocean heat content and surface wind anomalies for the decadal time-scale from the control experiment of the coupled model. The sequence of maps depicts approximately one-half of a life cycle of the composite anomalies associated with the decadal sea surface temperature variability shown in Fig. 14. The ocean heat content anomalies are defined as the vertically integrated temperature anomaly over the model layer within the depth range of 69 to 237 m, with a contour interval of 30 degC m. For surface wind anomalies, a reference vector of 3 m s^{-1} is shown at the bottom of the figure. From Knutson and Manabe (1998).

to the corresponding variability associated with ENSO. The similarity appears to imply that the dynamical mechanism of the decadal variability is essentially similar to ENSO on the interannual time-scale as suggested by Zhang *et al.* (1997).

Figure 16 illustrates observed and simulated anomalies of sea level pressure (SLP) and SST over the extratropical North Pacific and North American regions at the warm

tropical/cold extratropical phase of the decadal variability. The agreement between simulated and observed anomalies is fairly good with intensified Aleutian low and cold SST anomalies near 40°N. In both the observed and simulated composites, the strengthened Aleutian low, the weaker positive SLP anomalies over North America, and the negative SLP anomalies near the east coast of North America yield an overall pattern reminiscent of the Pacific–North American pattern described by Wallace and Gutzler (1981).

Figure 16 indicates that the cold SST anomalies in the North Pacific are located in regions of northerly surface wind anomalies. An analysis of the model's surface heat budget conducted by Knutson and Manabe (1998) suggests that these cold SST anomalies are a remote response to the warm, tropical SST anomalies through the so called 'atmospheric bridge'. They found that, on the decadal scale, the simulated cold SST anomalies associated with the decadal variation result in a large part from the thermal advection by near-surface current induced by the extratropical surface wind anomalies. This is in contrast to the simulated atmospheric bridge associated with interannual ENSO, in which the extratropical anomalies are produced mainly by surface heat flux variations.

Deser and Blackmon (1995) conducted an EOF analysis of winter SST in the Pacific Ocean (60°N–20°S). In the left-hand side of Fig. 17, the first two modes from their analysis are shown. The first mode explains 43% of the variance and resembles the simulated pattern of decadal variability discussed above. The second mode explains 11% of the variance, and is associated with the anomalies of SLP, which resemble the Pacific–North American pattern mentioned earlier. A similar pattern of decadal SST variability has been found from the analysis of the model data described earlier (not shown). In the right-hand side of the figure, the time series of the two winter SST anomalies indices, which are correlated very well with the two EOF modes already identified, are shown. Both time series appear to contain fluctuations of decadal as well as interannual time-scales. In addition, the tropical SST index of the first mode has a positive trend, whereas the extratropical SST index of the second mode exhibits a negative trend. The existence of these trends imply that both modes vary such that SST anomalies in the extratropical North Pacific become more negative with time during the second half of the twentieth century.

In conclusion, it appears that the cooling trend in the extratropical North Pacific is attributable partly to decadal-scale tropical variability that resembles ENSO apart from having a longer time-scale. In addition, the second EOF mode associated with the Pacific–North American pattern of SLP may have contributed substantially to the cooling trend. (As will be shown later, the GFDL* climate model has difficulty in fully reproducing the strong cooling trend in the North Pacific, when forced by greenhouse gases and sulphate aerosols.)

5. SIMULATED VARIABILITY OF TREND

Using a version of the coupled model which has the same medium resolution as the model used by Knutson and Manabe (1998), Knutson *et al.* (1999) recently attempted to simulate the pattern of observed surface temperature trends shown, for example, in Fig. 2. They conducted two types of numerical time integrations of the model with and without the combined radiative forcing of greenhouse gases and anthropogenic sulphate aerosols. Based upon the analysis of these experiments, they assessed the likelihood that the model can simulate the local trends of surface temperature observed during

* Geophysical Fluid Dynamics Laboratory.

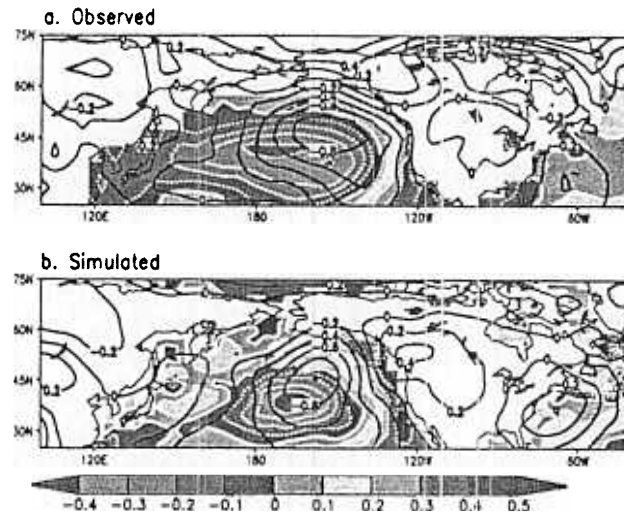


Figure 16. Composite decadal sea surface temperature (SST) (shading, white contours) and sea level pressure (SLP, dark contours) anomalies over the extratropical North Pacific and North America for the warm tropical/cool extratropical phase of decadal variability. Results are shown for (a) observation and (b) the coupled model. The contour interval is 0.1 degC for SST and 0.2 mb for SLP. From Knutson and Manabe (1998).

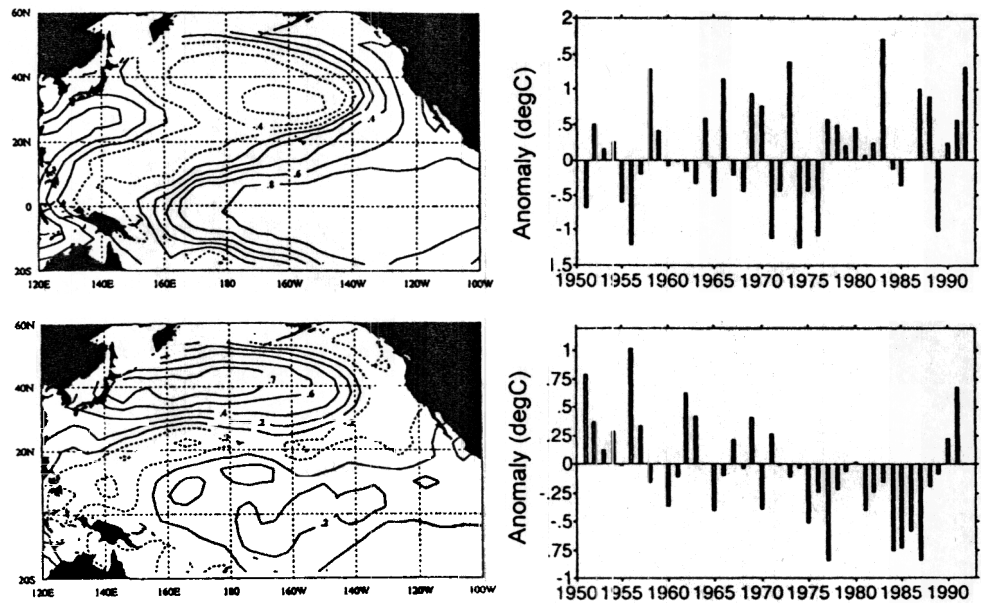


Figure 17. (a) and (b) Illustration of the first, and second empirical orthogonal function (EOF) modes of Pacific sea surface temperature (SST) respectively, based on winter anomalies during the period 1950/51–1991/92. The EOF is based on the covariance matrix and is shown in normalized form (i.e. correlation coefficient between the time series of the EOF and the original data). The contour interval is 0.2 and negative contours are dashed. (c) and (d) Illustration of the time series of winter SST anomalies averaged over the centre of action of the first EOF mode (equatorial Pacific SST index, 6°N–6°S, 178°W–106°W), and that of the second EOF modes (North Pacific SST index, 46°N–32°N, 136°E–176°W), respectively. The correlation coefficient between the SST index and the corresponding (rotated) EOF time series is 0.97 for both EOFs. From Deser and Blackmon (1995).

the latter half of the twentieth century. In the first subsection, we shall evaluate the unforced, 1000-year control integration of the model without radiative forcing. In the second subsection, this will be followed by an assessment based upon the results from an ensemble of five integrations of the model under the influence of the radiative forcing.

(a) *Unforced trends*

In general, the medium-resolution coupled model can simulate the variability of local and global surface temperature with skill that is comparable with or slightly better than the low-resolution coupled model described earlier.

Figure 18(b) compares the range of simulated trends with the observed trends of annual mean surface temperature shown in Fig. 18(a). The region with grey shading indicates the grid boxes where the observed trend (1949–97) is within the range between the maximum and minimum 49-year trend simulated in the last 900 years of the control integration of the model. According to the model simulations, the large observed warming trend over Alaska, as well as most of the continental region, is inside the maximum/minimum range of simulated trends. However, the large warming trend over extensive regions of Siberia and the modest warming trends over the Indian, eastern tropical Pacific, and South Atlantic Oceans are outside the maximum/minimum range simulated by the model. Thus, warming trends in these regions may be due, at least in part, to a sustained thermal forcing.

(b) *Forced trend*

Using the same model, Knutson *et al.* conducted an ensemble of five integrations forced by the combined radiative forcing of greenhouse gases and anthropogenic sulphate aerosols. The forcing used for these experiments is described by Haywood *et al.* (1997), and is practically identical in magnitude to the forcing employed by Mitchell *et al.* (1995) in their global warming experiments. The initial conditions for the ensemble of experiments were taken from the control integration, which was continued over a period of 1000 years.

Figure 19 illustrates the time series of global mean surface temperature, which is obtained from the ensemble of the five integrations forced by the radiative forcing identified earlier. For comparison, the time series of observed global mean surface temperature anomalies (Jones 1994; Parker *et al.* 1995) is also added to the same figure. The results indicate that the five simulated time series of global mean surface temperature anomalies generally track the observed warming trend during the twentieth century. In sharp contrast, the unforced control experiment fails to generate a sustained global warming trend such as that observed during the twentieth century. Thus, the analysis presented here underscores the conclusion discussed earlier that the observed warming trend is radiatively forced, at least in part, and cannot be generated by an internal mechanism alone.

Encouraged by the successful simulation of global surface temperature just described, Knutson *et al.* assess again the observed trends of local SAT (1949–97) based upon the analysis of an ensemble of the radiatively forced model integrations. Figure 18(c) illustrates the likelihood of realizing the observed local trend under the influence of the radiative forcing. Assuming that the climate-change signal and the internal variability are linearly additive, the distributions of forced trends used here are obtained by linearly combining the internal variability from the last 900 years of the control run with the ensemble mean trends from the forced experiments.

In this figure, the region with grey shading identifies the grid boxes where the observed trend is within the minimum to maximum range of the forced trends thus

determined. Colour-shaded (non-grey) contoured regions denote grid boxes where the observed trend is outside of the simulated ranges. Knutson *et al.* have evaluated the field significance of the difference between the observed and simulated trends following Livezey and Chen (1983). The differences between the ensemble forced trends and observed trends were found to exceed that expected due to chance alone at the 0.05 global significance level.

With the exception of the central North Pacific, the tropical Atlantic Ocean, and in the vicinity of New Zealand, the local trends of surface temperature observed during the last half century are within the maximum/minimum range of trends which are simulated by the medium-resolution model with radiative forcing. Possible reasons for the regional discrepancies over the Pacific and Atlantic Oceans identified earlier are discussed by Knutson *et al.* (1999). Nonetheless, the agreement between the simulated and observed trends is better for the simulations with greenhouse gases and sulphate aerosols than for the unforced simulations. For example, the large warming trend over Siberia and modest warming trend over the Indian Ocean, which were outside the maximum/minimum range of the control integration, are now inside the range of the radiatively forced integrations. It appears that the warming trend in these regions cannot be generated by the internal mechanism alone, but is induced at least partly by the increasing concentration of greenhouse gases in the atmosphere.

6. CONCLUSIONS

Over most of the globe, a coupled model such as that developed at the GFDL/NOAA simulates reasonably well the observed low-frequency variability of local surface temperature. One can make a similar statement for the mixed-layer model, which is constructed by combining an atmospheric GCM and a simple mixed-layer ocean model without the effect of oceanic heat transport. Hasselmann (1976) conjectured that SST variability of a mixed-layer ocean away from coastal boundaries could be regarded as a red-noise response to random daily weather disturbances. With the exception of certain oceanic regions such as the tropical Pacific, where ENSO predominates, this linear stochastic model appears to explain a major fraction of the low-frequency variability of surface temperature over most of the globe, including continents.

Based upon the analysis of observed and simulated time series of global mean surface temperature, Stouffer *et al.* (1994) concluded that it is not likely that the global warming trend of 0.5 degC per 100 years, which has been sustained during the twentieth century, is attributable solely to internal variability. Instead, they believe that it is induced, at least partly, by radiative forcing such as increasing concentrations of greenhouse gases in the atmosphere. This conclusion is clearly consistent with the well-known statement of the Intergovernmental Panel on Climate Change (1996): 'The balance of evidence suggests a discernible human influence on global climate'.

The observed trend of surface temperature over the last half century has been positive over most of the globe, with particularly large warming over and around Alaska and Siberia. However, a cooling trend of significant magnitude is notable over the northern North Atlantic and North Pacific Oceans.

Based upon the analysis of long-term integrations of the coupled model, it is suggested that the cooling trend around the Denmark Strait results from the variation of the East Greenland Current, which see-saws with the North Atlantic Current at multidecadal time-scales. The spectrum of simulated SST at the Denmark Strait has a statistically significant peak above the red-noise spectrum around the period of 60 years, deviating significantly from the linear stochastic model of Hasselmann.

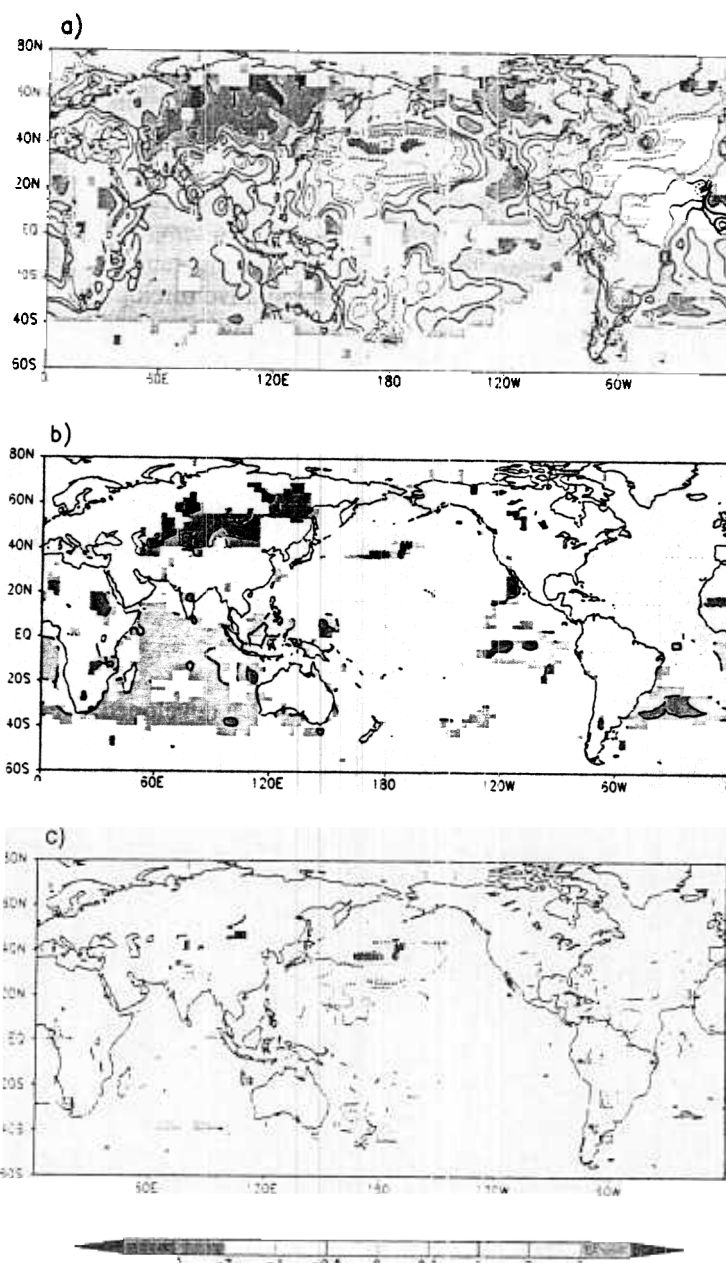


Figure 18. (a) Observed linear trends of annual mean surface temperature (Jones 1994; Parker *et al.* 1995) plotted with a contour interval of 1 degC per 100 years along with ± 0.5 degC per 100-year contours (negative contours shown dashed). White regions denote grid boxes where the observed data coverage was found to be insufficient. (b) Grey shading denotes grid boxes where the observed trend in annual mean surface temperature is within the minimum to maximum range as realized during the last 900-year period of the 1000-year control integration of the medium-resolution coupled model. Colour shaded (non-grey), contoured regions denote grid boxes where the observed trend is outside the simulated ranges, with the colour and contouring indicating the magnitude of the observed trend as illustrated in (a). (c) Same as (b) except that the observed trends are compared with the minimum to maximum range of trends which are obtained by adding the radiatively forced ensemble mean trend to the unforced trend distribution which is obtained from the control integration of the coupled model. From Knutson *et al.* (1999).

CLIMATE VARIATION

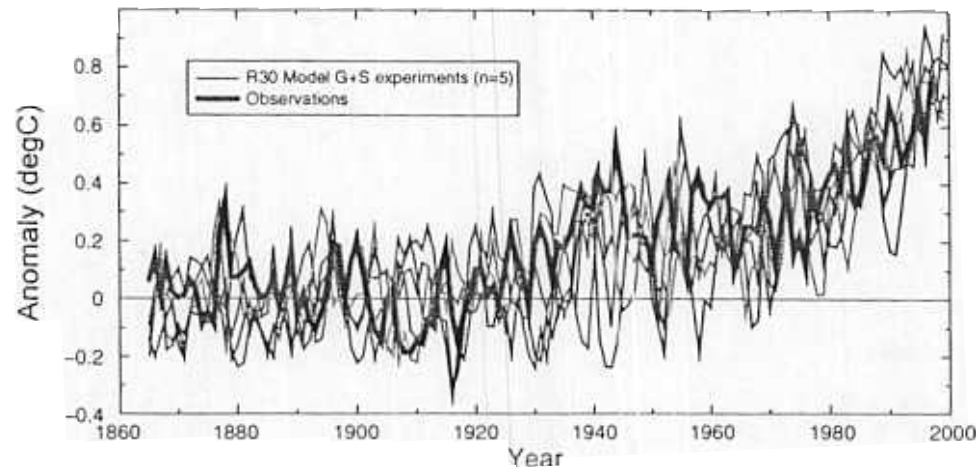


Figure 19. Globally averaged, annual mean surface temperature anomalies from 1865 to present based on observations (thick black curve), and an ensemble of five integrations of the coupled model under the influence of combined radiative forcing of increasing greenhouse gases and anthropogenic sulphate aerosols (thinner curves, various colours). The global mean anomalies are relative to the 1880–1920 base period. From Knutson *et al.* (1999).

It is also suggested that the cooling trend in middle latitudes of the North Pacific Ocean is attributable partly to the decadal variation of SST associated with an ENSO-like variability on decadal time-scales, which is simulated reasonably well by a version of the coupled model with medium resolution. It appears that, during the last few decades, the decadal variability is in the El Niño-like phase, with warm SST anomalies in the eastern tropical Pacific. The warm tropical anomalies in turn generate a train of wave disturbances in the atmosphere, which induces cold SST anomalies in the extratropical North Pacific, contributing to the cooling trend during the latter half of this century.

In addition to the decadal ENSO-like variability just described, the coupled model simulates another mode of decadal variability over the extratropical Pacific. The analysis of Deser and Blackmon (1995) suggests that this extratropical mode also contributes significantly to the cooling trend in the North Pacific Ocean.

In the circumpolar ocean of the southern hemisphere, the spectral density of simulated SST anomalies is significantly above the red-noise spectrum at multidecadal to centennial time-scales (Manabe and Stouffer 1996). As is the case with oceanic regions in high latitudes of the northern hemisphere, thermal advection by ocean currents helps generate SST anomalies in the circumpolar ocean, again deviating significantly from the linear stochastic theory (Hall and Manabe 1997).

Although surface temperature variability of the coupled model appears to be consistent with the linear stochastic theory of Hasselmann over a major fraction of the globe, it may not necessarily be so over high-latitude oceans at decadal to centennial time-scales as noted earlier. The theory does not apply to the tropical Pacific, where ENSO of interannual and decadal scales predominates. In the western boundary currents and circumpolar currents of the southern hemisphere, where mesoscale eddies are active, the theory fails at seasonal time-scales. For a more detailed assessment of the linear stochastic theory, see the study of Hall and Manabe (1997), which is based upon the detailed analysis of data from weather stations and the outputs from the coupled model.

In order to assess the local surface temperature trends, which have been observed during the last 50 years, Knutson *et al.* (1999) conducted many time integrations of the coupled model. In the last 900 years of the control integration without external forcing, the observed local trends of surface temperature lie within the maximum/minimum range of simulated trends over 75% of the area analysed. When the radiative forcing due to both greenhouse gases and anthropogenic sulphate aerosols is included in the simulations, the observed local trends during the last half century lie inside the maximum/minimum range over 86% of the area analysed.

The coupled atmosphere–ocean–land–surface model employed here incorporates simple parametrizations of relevant physical processes. Nevertheless, it simulates reasonably well many features of low-frequency variability of surface temperature. However, our understanding of decadal climate variabilities is far from satisfactory, making it urgent to elucidate the physical mechanisms involved. Fortunately, the simplicity of parametrizations and relatively low resolution of the coupled model facilitate the interpretation of the results obtained from numerical experiments. Owing to the computational efficiency of the model, one can conduct many numerical experiments with modest expenditure of computer time. More than 30 years have passed since a coupled model was developed for the first time and was used for the study of climate (Manabe and Bryan 1969). A relatively simple coupled model such as that used here has become a very powerful tool for exploring the basic physical mechanisms responsible for natural and anthropogenic variation of climate.

In order to make a reliable projection of future climate change, major emphasis has been placed upon the development of very comprehensive models of the coupled atmosphere–ocean–land–surface system, which incorporate many physical, chemical, and biological processes. Unfortunately, our current knowledge on many of these processes is often very rudimentary and is not sufficient for the development of quantitatively realistic parametrizations. Thus, there is no guarantee that these complex models are realistic. On the other hand, their complexity has often made it very difficult to understand the results obtained. Therefore, it is highly desirable that comprehensive model projection of future climate be evaluated using a hierarchy of climate models with various degrees of complexity.

ACKNOWLEDGEMENTS

Thanks are due to Jerry D. Mahlman, the director of the Geophysical Fluid Dynamics Laboratory/NOAA, who has given very valuable advice and wholehearted support for the modelling studies discussed here. The support of Michael J. Spelman has been indispensable for the development and time integrations of various versions of the coupled model. Syukuro Manabe is grateful to Brian Hoskins, the president of the Royal Meteorological Society, who invited him to present the Symons Memorial Lecture; this gave him an excellent opportunity to talk about the topic in which he has been interested throughout his career. He is grateful to Taroh Matsuno, the Director General of the Frontier Research System for Global Change for his encouragement and support.

REFERENCES

- | | | |
|---|------|---|
| Bryan, K. and Lewis, L. | 1979 | A water mass model of world ocean. <i>J. Geophys. Res.</i> , 84 , 2503–2517 |
| Dansgaard, W., Johnson, J. Clausen, H. B. and Langway Jr, C. C. | 1971 | 'Climate record revealed by the Camp Century ice core'. Pp. 37–56 in <i>The late Cenozoic glacial ages</i> . Ed. K. K. Turekian. Yale University Press, New Haven, Conn., USA |

- Delworth, T. L. and Greatbatch, R. J. 2000 Multidecadal thermohaline circulation variability driven by atmospheric surface forcing. *J. Climate*, **13**, 1481–1495
- Delworth, T. L. and Mann, M. E. 2000 Observed and simulated multidecadal variability in the North Atlantic. *Clim. Dyn.*, **16**, 671–676
- Delworth, T. L., Manabe, S. and Stouffer, R. J. 1993 Interdecadal variation of the thermohaline circulation in a coupled ocean–atmosphere model. *J. Climate*, **6**, 1993–2011
- 1997 Multidecadal climate variability in the Greenland Sea and surrounding regions: a coupled model simulation. *Geophys. Res. Lett.*, **24**, 257–260
- Deser, C. and Blackmon, M. L. 1993 Surface climate variation over the North Atlantic Ocean during winter: 1900–1989. *J. Climate*, **6**, 1743–1753
- 1995 On the relationship between tropical and North Pacific sea surface temperature variations. *J. Climate*, **8**, 1677–1680
- Dickson, R. R., Meincke, J., Malberg, S.-A. and Lee, A. J. 1988 The ‘Great salinity anomaly’ in the northern North Atlantic 1968–1982. *Prog. Oceanogr.*, **20**, 103–151
- Dooley, H. D., Martin, J. H. A. and Ellet, D. J. 1984 Abnormal hydrographic conditions in the north-east Atlantic during the nineteen-seventies. *Rapport et Proces verbaux des Reunions du Conseil Permanent International pour l’Exploration de la Mer, Copenhague*, **185**, 179–187
- Gordon, C. T. and Stern, W. 1982 A description of the GFDL global spectral model. *Mon. Weather Rev.*, **110**, 625–640
- Gordon, C., Cooper, C., Senior, C. A., Banks, H., Gregory, J. M., Johns, T. C., Mitchell, J. F. B. and Wood, R. A. 2000 The simulation of SST, sea ice extent and ocean heat transport in a version of the Hadley Centre coupled model without flux adjustment. *Clim. Dyn.*, **16**, 147–168
- Gregory, J. M. and Mitchell, J. F. B. 1997 The climate response to Hadley Centre GCM with and without flux adjustment. *Geophys. Res. Lett.*, **24**, 1943–1946
- Hall, A. and Manabe, S. 1997 Can local linear stochastic theory explain sea surface temperature and salinity variability? *Clim. Dyn.*, **13**, 167–180
- Hansen, J., Ruedy, R., Glascoe, J. and Sato, M. 1999 GISS analysis of surface temperature change. *J. Geophys. Res.*, **30**, 30997–31022
- Hansen, J., Lacis, A., Rind, D., Russell, G., Stone, P., Fung, I., Ruedy, R. and Lerner, J. 1984 ‘Climate sensitivity: analysis of feedback mechanisms’. Pp. 130–163 in *Climate process and climate sensitivity*. Eds. J. E. Hansen and T. Takahashi. Maurice Ewing Series, Vol. 5. American Geophysical Union, Washington, D.C., USA
- Hasselmann, K. 1976 Stochastic climate models. Part I: Theory. *Tellus*, **28**, 473–485
- Haywood, J. M., Stouffer, R. J., Wetherald, R. T., Manabe, S. and Ramaswamy, V. 1997 Transient response of a coupled model to estimated changes in greenhouse gas and sulfate concentrations. *Geophys. Res. Lett.*, **24**, 1335–1338
- Intergovernmental Panel on Climate Change 1996 *Climate change 1995: The science of climate change*. Cambridge University Press
- Jones, P. and Wigley, T. M. L. 1991 ‘Global and hemispheric anomalies’. Pp. 512–517 in *Trend ‘91: A compendium of data on global change*. Eds. T. A. Boden, R. J. Sepanski, and F. W. Stoss. Oak Ridge National Laboratory, USA
- Jones, P. D. 1994 Hemispheric surface temperature variations: A reanalysis and update to 1993. *J. Climate*, **7**, 1794–1802
- Knutson, T. R. and Manabe, S. 1998 Model assessment of decadal variability in the tropical Pacific Ocean. *J. Climate*, **11**, 2273–2296
- Knutson, T. R., Manabe, S. and Gu, D. 1997 Simulated ENSO in a global coupled ocean–atmosphere model: Multidecadal modulation and CO₂ sensitivity. *J. Climate*, **10**, 138–161
- Knutson, T. R., Delworth, T. L., Dixon, K. W. and Stouffer, R. J. 1999 Model assessment of regional surface temperature trends. *J. Geophys. Res.*, **104**, 30981–30996
- Kushnir, Y. 1994 Interdecadal variation in North Atlantic sea surface temperature and associated atmospheric conditions. *J. Climate*, **7**, 141–157
- Livezey, R. E. and Chen, W. Y. 1983 Statistical field significance and its determination by Monte Carlo techniques. *Mon. Weather Rev.*, **111**, 46–59
- Manabe, S. and Bryan, K. 1969 Climate calculation with a combined ocean–atmosphere model. *J. Atmos. Sci.*, **26**, 785–789
- Manabe, S. and Stouffer, R. J. 1996 Low frequency variability of surface air temperature in a 1000-yr integration of a coupled atmosphere–ocean–land surface model. *J. Climate*, **9**, 376–393

- Manabe, S. and Stouffer, R. J. 1999 The role of thermohaline circulation in climate. *Tellus*, **51** A-B, 91–101
- Manabe, S., Smagorinsky, J. and Strickler, R. F. 1965 Simulated climatology of a general circulation model with a hydrologic cycle. *Mon. Weather Rev.*, **93**, 769–798
- Manabe, S., Stouffer, R. J., Spelman, M. J. and Bryan, K. 1991 Transient response of a coupled ocean–atmosphere model to gradual changes of atmospheric CO₂. Part I: Annual mean response. *J. Climate*, **4**, 785–818
- Mitchell, J. F. B., Johns, T. C., Gregory, J. M. and Tett, S. F. B. 1995 Climate response to increasing level of greenhouse gases and sulphate aerosols. *Nature*, **376**, 501–504
- Parker, D. E., Folland, C. K. and Jackson, M. 1995 Marine surface temperature: Observed variation and data requirements. *Clim. Change*, **31**, 559–600
- Rayner, N. A., Horton, E. B., Parker, D. E., Folland, C. K. and Hackett, R. B. 1996 'Version 2.2 of the global sea ice and sea surface temperature data set, 1903–1994'. UKMO Climate Research Tech. Note CRTN74. (Available from the National Meteorological Library, Meteorological Office, London Rd., Bracknell, Berkshire RG12 2SY, UK)
- Reynolds, R. W. and Smith, T. W. 1994 Improved global sea surface temperature analysis. *J. Climate*, **7**, 929–948
- Smith, T. M., Reynolds, R. W., Livezey, R. E. and Stokes, D. C. 1996 Reconstruction of historical sea surface temperature using empirical orthogonal functions. *J. Climate*, **9**, 1403–1420
- Stouffer, R. J., Manabe, S. and Vinnikov, K. Ya. 1994 Model assessment of the role of natural variability in recent global warming. *Nature*, **367**, 634–636
- Stouffer, R. J., Hergerl, G. and Tett, S. 2000 A comparison of surface air temperature variability in three 1000-yr coupled ocean–atmosphere model integrations. *J. Climate*, **13**, 513–537
- Wallace, M. and Gutzler, D. S. 1981 Teleconnection in the geopotential height field during the northern hemisphere winter. *Mon. Weather Rev.*, **109**, 784–812
- Zhang, Y., Wallace, J. M. and Battisti, D. S. 1997 ENSO-like interdecadal variability: 1900–93. *J. Climate*, **10**, 1004–1020